Foreshocks during the nucleation of stick-slip instability

Gregory C. McLaskey[1] and Brian D. Kilgore[1]

[1]   We report on laboratory experiments which investigate interactions between aseismic slip, stress changes, and seismicity on a critically stressed fault during the nucleation of stick-slip instability. We monitor quasi-static and dynamic changes in local shear stress and fault slip with arrays of gages deployed along a simulated strike-slip fault (2 m long and 0.4 m deep) in a saw cut sample of Sierra White granite. With 14 piezoelectric sensors, we simultaneously monitor seismic signals produced during the nucleation phase and subsequent dynamic rupture. We observe localized aseismic fault slip in an approximately meter-sized zone in the center of the fault, while the ends of the fault remain locked. Clusters of high-frequency foreshocks ($M_w \sim -6.5$ to -5.0) can occur in this slowly slipping zone 5–50 ms prior to the initiation of dynamic rupture; their occurrence appears to be dependent on the rate at which local shear stress is applied to the fault. The meter-sized nucleation zone is generally consistent with theoretical estimates, but source radii of the foreshocks (2 to 70 mm) are 1 to 2 orders of magnitude smaller than the theoretical minimum length scale over which earthquake nucleation can occur. We propose that frictional stability and the transition between seismic and aseismic slip are modulated by local stressing rate and that fault sections, which would typically slip aseismically, may radiate seismic waves if they are rapidly stressed. Fault behavior of this type may provide physical insight into the mechanics of foreshocks, tremor, repeating earthquake sequences, and a minimum earthquake source dimension.

1.   Introduction

[2]   When a seismogenic fault begins to slip, its ability to resist continued sliding is weakened. This property of fault friction is thought to be what causes earthquake-generating slip instabilities to spontaneously develop on a slowly loaded fault, a process referred to as earthquake nucleation. The precise form of the slip-weakening friction behavior depends on the fault slip rate and the slip time history and can be modeled by the rate- and state-dependent friction equations [*Dieterich*, 1979; *Ruina*, 1983; *Marone*, 1998]. A number of numerical models use these rate and state equations to explore the length and time scales over which earthquake nucleation occurs and the manner in which it is affected by changes in friction properties, loading rates, and stress heterogeneities [*Dieterich*, 1992; *Lapusta and Rice*, 2003; *Rubin and Ampuero*, 2005; *Ampuero and Rubin*, 2008; *Kaneko and Lapusta*, 2008; *Fang et al.*, 2010]. The models show that the rapid, unstable, and inertially controlled fault slip that generates earthquakes is always preceded by quasi-stable and presumably aseismic but accelerating slip on a localized section of the fault referred to here as the nucleation zone.

This modeling effort has been successful in explaining similar phenomena reported in laboratory experiments [e.g., *Dieterich* 1978; *Okubo and Dieterich*, 1984; *Ohnaka and Kuwahara* 1990]. When the rate-state nucleation models employ laboratory values of friction parameters, they suggest that earthquake nucleation zones could be as small as 1 m and any expansion occurs only in the final millisecond prior to the earthquake [*Tullis*, 1996; *Kaneko and Lapusta*, 2008; *Fang et al.*, 2010]. If the models and the friction parameters they employ are applicable to natural faults, the possibility of detecting premonitory processes is remote. The lack of any observable seismicity or significant premonitory stress changes in the hours to minutes before the 2004 Parkfield earthquake [*Johnston et al.*, 2006] reinforced the view that nucleation processes are small and difficult, if not impossible, to detect. But the reliable extrapolation of friction parameters to values relevant for natural faults remains a subject of debate.

[3]   If a similar nucleation zone exists on natural faults and spans many kilometers and aseismic slip accelerates over many hours, then it might be detectable either by physical or chemical changes, such as fluid movement or ground deformation, or by foreshocks or other seismic activity associated with the premonitory slip [see, e.g., *Dieterich*, 1978; *Geller*, 1997]. In some cases, clusters or swarms of small earthquakes have been detected within a few kilometers of the eventual hypocenter of a main shock in the weeks to seconds before earthquakes [e.g., *Dodge et al.* 1995, 1996, *Zanzerkia et al.*, 2003, *Bouchon et al.*, 2011,

---

[1]United States Geological Survey, Menlo Park, California, USA.

Corresponding author: G. C. McLaskey, United States Geological Survey, 345 Middlefield Rd., MS 977, Menlo Park, CA 94025, USA. (gmclaskey@usgs.gov)
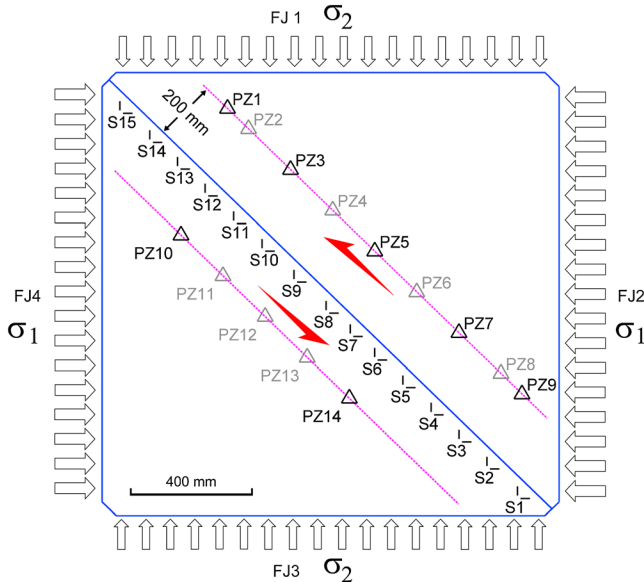
Figure 1. Schematic diagram of top view of the sample and sensor locations. Pressure from the flat jacks (FJ1–FJ4) causes the 2 m long fault cut diagonally through the sample to slip in left-lateral shear. The black and gray triangles denote the locations of piezoelectric sensors (PZ1–PZ14) on the top and bottom sample surfaces, respectively. In addition to the 15 strain gage pairs located along the top of the fault (S1–S15), three pairs of strain gages (S16–S18) are located on the bottom of the sample directly underneath S15, S8, and S1, respectively. Fourteen slip sensors straddle the fault trace and are essentially collocated with the strain gage pairs.

Chiaraluce et al., 2011, *Miyazaki et al.*, 2011; *Ando and Imanishi*, 2011; *Marsan and Enescu*, 2012; *Tape et al.*, 2013]. While they are termed foreshocks, the precise physical connection between foreshocks and main shocks is not well established. Not all large earthquakes appear to be preceded by smaller ones, and not all earthquake swarms produce a main shock. It is not clear whether foreshocks trigger the main shock or are a by-product of the main shock nucleation process. Nevertheless, foreshocks appear to be much more common along oceanic transform faults, where seismic coupling is lower, and more interplate motion appears to be accommodated aseismically [*McGuire et al.* 2005; *Boettcher and McGuire*, 2009]. If foreshocks are a seismically detectable component of the earthquake nucleation process, then it would be useful to better understand the physics and mechanics of their creation and the information they provide about nucleation-related stress changes pertinent to operational earthquake forecasting.

[4] In the rate-state nucleation models outlined above, the beginning of the seismically detectable portion of an earthquake is poorly or arbitrarily defined. Many modelers choose a slip speed of 0.1 m/s as the threshold between aseismic and seismic. In most cases, the model results are not dependent on this choice because slip exponentially accelerates to produce an earthquake. But an increasing number of studies show a complicated interplay between slow and presumably aseismic slip and more rapid, potentially seismic slip [*Lapusta and Liu*, 2009; *Lengline et al.*, 2012; *Ghosh et al.*, 2012]. A better understanding of the transition from aseismic

to seismic slip may allow us to more intelligently use small earthquakes, tectonic tremor [*Obara* 2002], and low-frequency earthquakes [e.g., *Shelly et al.*, 2006] as indicators of underlying aseismic processes and might allow initial P wave signatures of larger earthquakes to be more effectively used for earthquake early warning systems [*Ellsworth and Beroza*, 1995; *Lewis and Ben-Zion*, 2007].

[5] In this paper, we report on laboratory experiments conducted on a densely instrumented, large-scale simulated strike-slip fault in order to study the initiation of a stick-slip instability, which is thought to be analogous to earthquake nucleation. We monitor local stress changes and premonitory fault creep at many locations along the fault throughout many stick-slip cycles, and we use piezoelectric sensors to monitor foreshocks and other seismic signals that are produced during nucleation. The repeated stick-slip of the same sample under nearly identical loading conditions is intended to simulate the earthquake cycle.

[6] Consistent with previous nucleation experiments [*Dieterich* 1978; *Okubo and Dieterich* 1984; *Ohnaka and Kuwahara*, 1990; *Ohnaka and Shen*, 1999; *Nielsen et al.*, 2010; *Beeler et al.*, 2012], we detect a localized zone of quasi-stable slip that precedes rapid slip across the entire laboratory fault. We find that foreshocks occur within this zone but only during the late stages of nucleation when local stresses vary rapidly. Similar to repeating earthquakes [e.g., *Nadeau and Johnson*, 1998; *Beeler et al.*, 2001] and persistent radiators of tremor [*Ghosh et al.*, 2012], the locations of foreshocks persistently cluster on small seismogenic patches of the laboratory fault while other fault sections slip aseismically or remain locked during the nucleation stages. By tracking specific sequences of foreshocks over many stick-slip cycles, we find that those fault patches that persistently produce foreshocks will slip aseismically when nucleation proceeds at a slower rate.

[7] The foreshocks we record are significantly smaller than the theoretical minimum length scale h^* over which an earthquake can nucleate under conditions of quasi-static loading and homogeneous fault friction [*Dieterich*, 1986; *Rice*, 1993; *Lapusta and Rice*, 2003]. In section 4, we explore possible causes of this discrepancy, including the relevance of the fault constitutive law and the potential contribution of fault heterogeneity. We find that heterogeneity of fault strength is a necessary but not sufficient condition for the production of the observed $M_w \sim -5$ to -6.5 foreshocks. We find that these tiny earthquakes cannot nucleate on their own but only occur when accelerating aseismic fault slip causes local shear stressing rates to increase many orders of magnitude above the externally applied rate. These observations suggest that frictional stability is modulated by local stressing rate and that earthquakes smaller than h^* can occur under rapid loading conditions.

2. Description of the Laboratory Experiments

2.1. Test Procedure

[8] The 1.5 m square and 0.419 m thick sample of Sierra white granite is from a quarry in Raymond, California, and is described schematically in Figure 1. A 2 m long fault is cut diagonally through the sample. Four flat jacks (FJ1–FJ4) apply pressure to the four side edges of the sample to generate σ_1 and σ_2, the principle stresses on the fault surface.
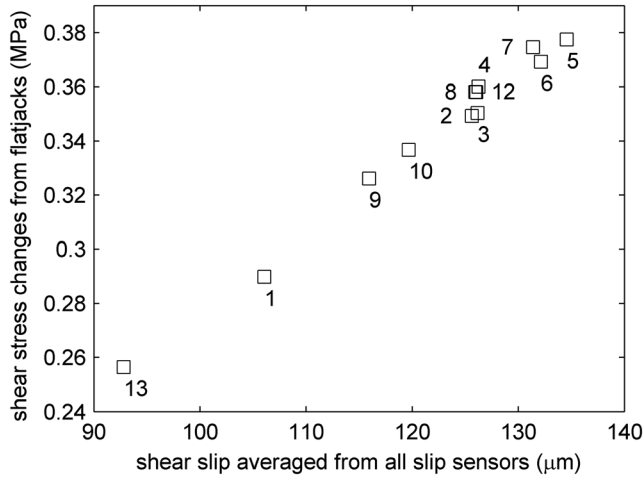
Figure 2. The squares mark the sample-averaged fault slip and stress changes from events in a sequence of stick-slip events recorded in January 2012. The slope of the line that the data points make with the origin is equal to the apparatus stiffness. Comparison with Figure 6 shows that events with high stress changes and slip nucleated faster than those with low stress changes.

By means of a servo-hydraulic system, the pressure in FJ1 and FJ3 is slowly decreased while pressure in FJ2 and FJ4 is increased such that fault normal stress remains constant at 5 MPa while shear stress is slowly increased at a rate of 0.001 MPa/s. Under these conditions, stick-slip instabilities occur at about 3.7 MPa of shear stress, during which the entire fault slips about 125 μm, and sample-averaged stress change (derived from pressure in the flat jacks) is about 0.35 MPa. Sample-averaged fault slip and stress changes for a sequence of stick-slip events are shown in Figure 2. From this, we determine the apparatus stiffness to be about 2.5 kN/μm (0.003 MPa/μm).

[9] Figure 3a shows shear stress over three stick-slip cycles and describes the four stages of the experiment: loading, the stick-slip instability, reset, and hold. These stages are repeated to produce sequences of stick-slip events. Events from a sequence performed in January 2012 are denoted as $SE1_{Jan2012}$ to $SE13_{Jan2012}$ while those from a sequence conducted in November 2011 are denoted $SE1_{Nov2011}$ to $SE6_{Nov2011}$. In the reset stage, shear stress (as measured from the flat jacks) is reduced to 2.5 MPa. The reset stage was omitted prior to events $SE8_{Jan2012}$ to $SE13_{Jan2012}$, and the sample was reloaded from the residual stress level (τ_{ss}) left by the previous stick-slip event. Externally applied shear stressing rate is constant at 0.001 MPa/s, so variations in recurrence time between slip events are due to variations in t_{hold}, τ_{ss}, τ_p, and the reset stage (see Figure 3a). Here τ_p denotes the maximum average shear stress level. On average, interevent times are ~25 min for stick-slip events preceded by a reset stage and ~8 min for those without reset.

2.2. Instrumentation

[10] The top surface of the sample is instrumented with 14 slip sensors that straddle the fault and measure local fault slip at ~100 nm resolution. Local shear stress is derived from measurements from 18 strain gage pairs oriented at 45° and 135° from the fault trace. A set of 15 pairs of strain gages

(S1–S15) are mounted 13 ± 2 mm from the top trace of the fault and three pairs, S16–S18, are located at the same distance from the fault but on the underside of the sample directly beneath S15, S8, and S1, respectively. Instrument locations are shown in Figure 1. An array of 14 Panametrics V103 piezoelectric sensors (PZ1-PZ14) are mounted 200 mm from the fault on either side of the fault and on both the top and bottom surfaces of the sample. These sensors detect vertical motion (normal to the top and bottom surfaces of the sample) in the frequency range of ~100 Hz to ~1 MHz and act as vertical-component seismic stations. Because of their off-fault location and the finite thickness of the sample, the vertical motions detected by the piezoelectric sensors provide enough information to characterize seismic sources, including those from purely horizontal fault motion. Output from the slip and strain sensors is recorded continuously at 100 Hz and also recorded at 1 MHz for 500 ms surrounding each stick-slip event. Output from the 14 piezoelectric sensors is recorded at 5 MHz for 100 ms surrounding each stick-slip event and was simultaneously digitized at two different ranges. A large digitization range was used to capture, on scale, the full strong motions during dynamic rupture, and a smaller digitization range was used to record the tiny foreshocks at higher resolution during the initiation of rupture. We also continuously record the externally applied normal and shear stresses on the fault, which are derived from the hydraulic pressure measured in the flat jacks. More experimental details about the apparatus, slip sensors, and strain gages can be found in *Beeler et al.* [2012].

3. Results

3.1. Nucleation Stress Changes

[11] Throughout most of the loading stage, shear stress (derived from strain gage pairs S1–S18) increases in a near-linear fashion at every measured location on the block; but tens of seconds prior to the stick-slip instability, local shear stress at many of the sensor locations departs significantly from linearity, as shown in Figure 3b. Externally applied stress levels across the whole fault are constantly increasing at 0.001 MPa/s throughout the loading stage, so this departure from linearity indicates that some portion of the fault is slipping. This stress redistribution and premonitory fault slip accelerates as the time of the stick-slip instability grows near. In the final milliseconds before the stick-slip instability, local stressing rates measured at some of the strain gage locations are at least 20 MPa/s due to premonitory fault slip at neighboring locations. After a certain point in the cycle (probably the beginning of nucleation phase ii, described below), nucleation is driven entirely by elastic energy stored in the sample; it is self-driven and is not directly controlled by the external loading rate [*Dieterich and Kilgore*, 1996].

[12] Figure 4 shows local shear stress on a logarithmic time scale at three representative locations: the top center of the fault, the bottom center, and near the end of the fault. We use local maxima of the shear stress versus time to instability curve (shown as arrows in Figure 4) to mark phases in the nucleation process. Figure 5 shows a cartoon of the approximate locations of slipping regions and the expansion of the slipping front during these phases. We define the beginning of phase i as the time of the departure from linearity of the local shear stress at S8 near the top center of the fault (also shown in Figure 3b), which occurs tens of seconds
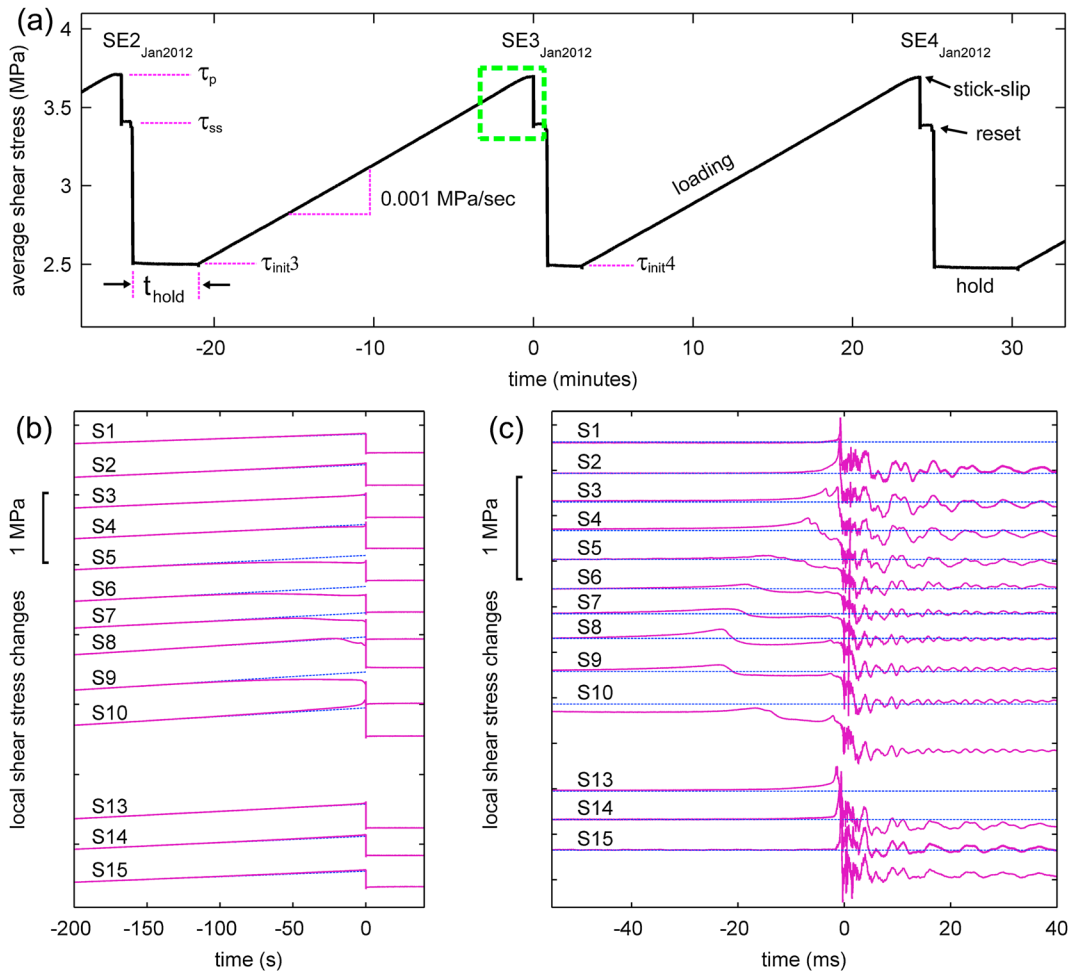
Figure 3. Stages of the stick-slip experiments and associated stress changes. (a) The four stages of the experiment—loading, stick-slip instability, reset, and hold—are illustrated via changes in the average of shear stress measurements made at many locations along the fault. Repetition of these stages produces sequences of stick-slip events somewhat analogous to the earthquake cycle. (b) Local shear stress derived from strain gage pairs at many locations (S1–S15) along the top of the fault in the final minutes before stick-slip instability. The time window is shown as a dashed box in Figure 3a. Departure from linearity (reference lines shown as thin dotted lines) indicates local fault slip. Tens to hundreds of seconds before failure, in Figure 3b, local slip is heterogeneous at least to the 150 mm station spacing, but in the final tens of ms before instability. (c) Slip localizes to an approximately meter-scale nucleation zone in the center of the fault before rapidly and bilaterally expanding as a crack-like shear rupture. Note that the slope of the dotted reference lines in Figures 3b and 3c are identical, but the offsets in Figure 3c are adjusted for clarity.

before the stick-slip instability. In this phase, the center part of the fault slips (10–30 nm/s slip rates) while the fault ends remain locked (slip rates less than 1 nm/s). Total measured slip during this time does not typically exceed 1 μm, but slip rates measured by adjacent slip sensors (~150 mm apart) sometimes have slip rates that differ by about a factor of 3 and accumulate slip that differs by hundreds of nanometers, so we describe the slip distribution as heterogeneous rather than coherent. We define phase ii to begin when slip initiates at the bottom center of the block, which was previously locked. A distinct sequence of foreshocks is sometimes detected in this phase (described later) which indicates that the slipping region expands along strike and up toward the top surface. The fault slip near the bottom center of the fault sheds stress relatively rapidly back to the top center, and in phase iii, the top center of the fault begins to slip coherently

as a bilaterally expanding shear crack that propagates along strike. Stress concentrates at the edges of the slipping region which expands at a velocity that accelerates from ~20 m/s up to ~700 m/s. The beginning of phase iv, marked by a peak in local shear stress at S15, indicates that the slipping region has expanded to the fault end.

[13] Figure 6 shows local shear stress similar to that shown in Figure 4 but compares many different stick-slip instabilities. The nucleation of each stick-slip instability in the sequence can be described by a nearly identical sequence of phases, as described in Figures 4 and 5, but the timing of the phases varies from one stick-slip instability to the next. The stick-slip events are not shown in chronological order; they are arranged by the speed of their nucleation sequences from fastest to slowest. Figure 3 shows SE3$_{Jan2012}$, an example of a moderately slowly nucleating stick-slip event.
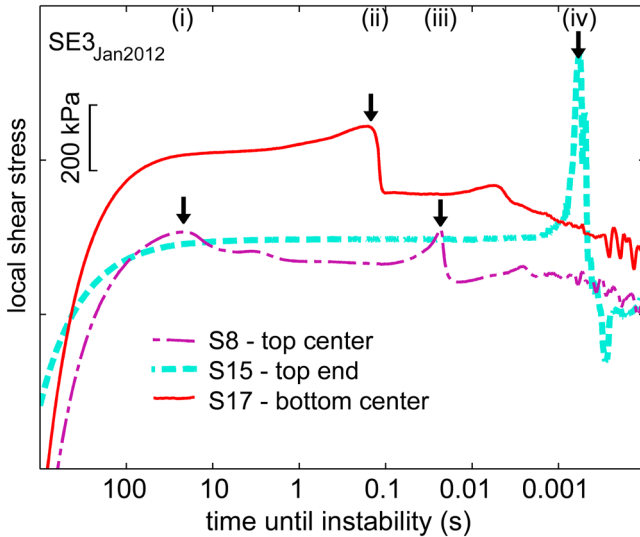
Figure 4. Local shear stress derived from strain gage pairs at three representative locations near the fault. Local maxima in the stress versus time to stick-slip instability curve are used to mark phases i–iv in the nucleation process. Stress is plotted on a log time scale so that these features can be identified even though local stressing rates rapidly accelerate in the last second before stick slip (despite the fact that externally applied stressing rate is held constant).

[14] Figure 7 shows local shear stress changes during nucleation phases iii and iv similar to Figure 3c but shows a zoom-in on the final milliseconds before the nucleation zone reaches the sample edges. The thick dashed lines indicate the approximate location of the rupture front as it accelerates from ~20 m/s to ~700 m/s. We compare a rapidly nucleating stick-slip instability (Figure 7a) to a slowly nucleating one (Figure 7b). Faster-nucleating stick-slip instabilities have smaller-sized nucleation zones and their expansion accelerates to a significant fraction (i.e., 25%) of the shear wave velocity before reaching the edge of the sample. Stick-slip instabilities that nucleate more slowly have larger nucleation zones. Slip rates measured on the top surface of the fault during this time increase from ~1 mm/s (~30 μm/s) up to ~20 mm/s (~1 mm/s) for the fastest (slowest) nucleating stick-slip instabilities. Once the accelerating rupture front reaches the sample edges, rupture fronts propagate along strike at velocities close to the shear wave speed. In this experiment, the physics and mechanics of dynamic rupture propagation and arrest depend, to a large extent, on the finite sample size and the properties of the testing apparatus. While useful insights into dynamic rupture behavior and the radiation of seismic energy can be made, this paper discusses only the nucleation and early propagation of fault slip that is confined to within the 2 m length of the fault. It is likely that the characteristics of nucleation phase iv are affected by end effects associated with the sample edges (such as reduced stiffness and reflections), but because of the variation in nucleation zone size and timing observed for different stick-slip events, we believe that the fault ends do not have a major effect on nucleation phases i to iii. Differences in the spatial extent and speed of nucleation are also apparent from the analysis of seismic waves, described in section 3.2.2.

[15] It should be noted that the size of the nucleation zone and the amount of preseismic slip are also thought to be a function of the roughness of the simulated fault [*Okubo and Dieterich*, 1984]. Previous work on this apparatus was conducted on one of two samples, which had simulated fault surfaces that were characterized as either "rough" (lapped with 30 grit abrasive producing 80 μm peak-to-trough roughness measured with a profilometer over a traverse of 2 cm) or "smooth" (240 grit abrasive, 0.2 μm roughness) [*Okubo and Dieterich*, 1984]. Very little preseismic slip was observed during similar experiments using the sample with a "smooth" fault [e.g., *Dieterich* 1981; *Lockner et al.*, 1982; *Lockner and Okubo*, 1983]. The current experiments were conducted on the sample with a "rough" fault, as described by others [*Okubo and Dieterich*, 1984; *Beeler et al.*, 2012]. High-frequency foreshocks probably also accompanied stick-slip events reported in previous work (including experiments conducted on the "smooth" fault sample), but it is unlikely that foreshocks similar to those reported here would have been detected without the current piezoelectric sensor array or without the dynamic range of the current high-speed recording system.

### 3.2. Ground Motions Recorded With Piezoelectric Sensors

[16] The seismic signals recorded with the piezoelectric sensor array span the full bandwidth and dynamic range of the sensors and recording system. They range from very low frequency ground deformations with 10 ms periods and longer to very high frequency motions with significant frequency content above 500 kHz.

3.2.1. High-Frequency Foreshocks

[17] Much of the seismicity recorded during the stick-slip nucleation has broadband frequency content (including very high frequencies up to hundreds of kHz) and shows
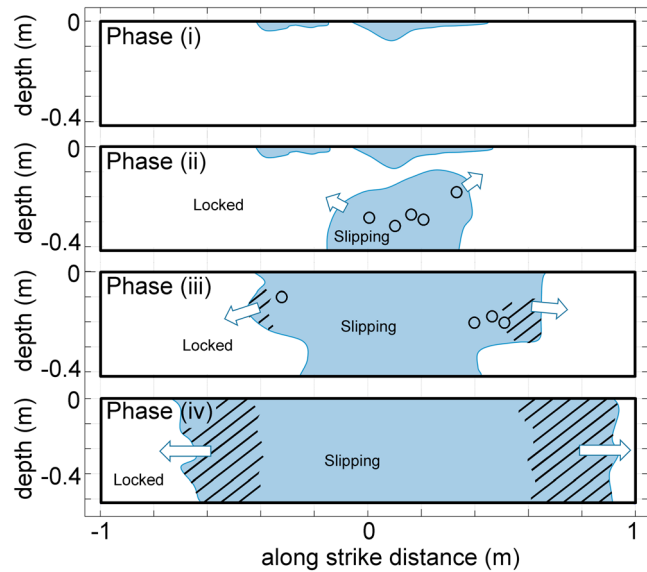
Figure 5. Cartoon showing fault cross sections and the approximate locations of slipping regions (shaded areas) and the expansion of the slipping front during nucleation. Circles and hatched regions denote the approximate locations of discrete foreshocks and more continuous radiation of high-frequency seismic waves, respectively.
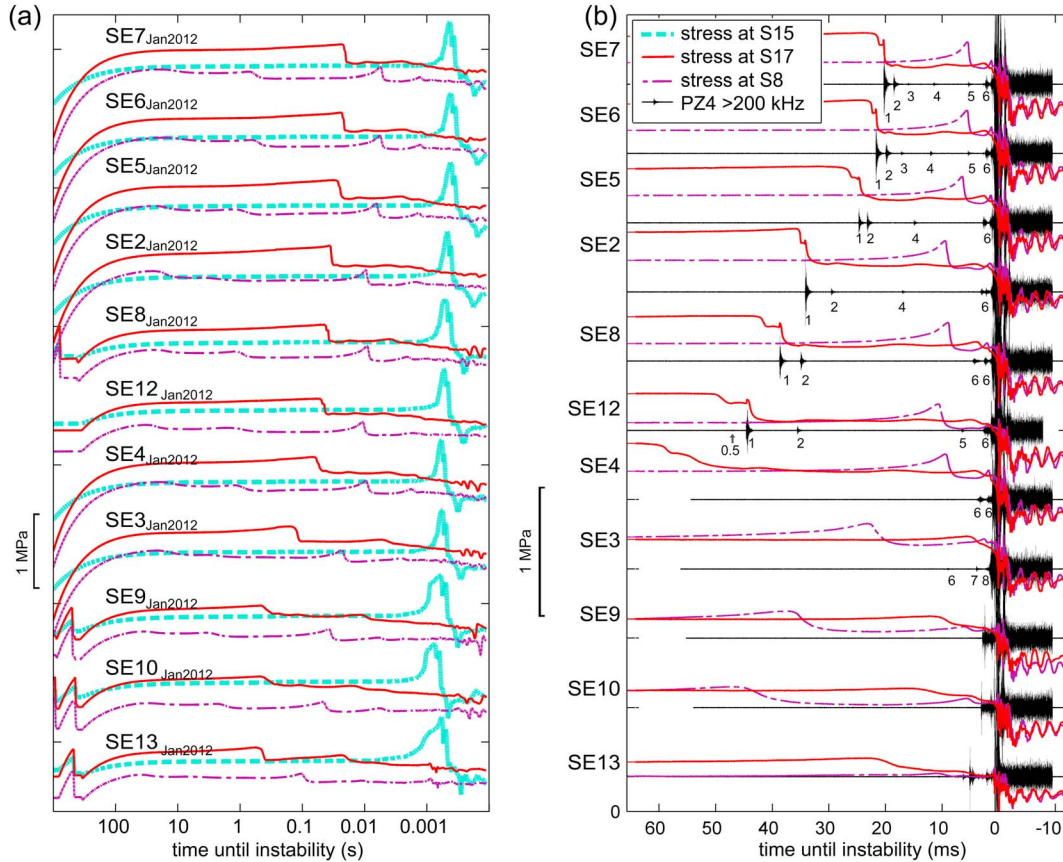
Figure 6. The stress redistribution during the nucleation of many different stick-slip instabilities. Each nucleation can be characterized by a nearly identical set of phases which are shown in Figure 4. The vast majority of the differences between the nucleation processes of the different stick-slip instabilities (labeled SE2–SE13) are in the timing of the phases. (a) Stress derived from strain gage pairs at three different locations on the samples is plotted as a function of the logarithm of time before the stick-slip instability. (b) A subset of the data from Figure 6a is plotted on a linear time scale alongside high-frequency ground motions recorded with piezoelectric sensor PZ4. The PZ4 data is high-pass filtered at 200 kHz to highlight the foreshocks which are sometimes observed during nucleation phase ii.

pulse-shaped P and S wave arrivals with short time duration ($\sim$3–25 μs pulse width). Under the simple assumption that rupture velocity is equal to the shear wave velocity in the granite, this puts an upper bound on source radius of 8–70 mm. The wavelengths of these high-frequency seismic waves are short compared to the observation distance, and this causes the seismic sources to resemble small earthquakes. For ease of discussion, they are termed foreshocks and they are analyzed using seismic source representation theorem in much the same way that typical earthquakes are studied. Attenuation is significant enough at $\sim$100 kHz frequencies that direct arrivals can be easily distinguished from reflections off the sides of the sample.

[18] Following the sensor calibration techniques of *McLaskey and Glaser* [2012], it was found that in the $\sim$50 kHz to 1 MHz frequency band, the signals from the piezoelectric sensors are nearly proportional to vertical ground displacement; the sensors introduce only mild distortion. At frequencies higher than 200 kHz, the wavelengths are comparable in length to the diameter of the cylindrical piezoelectric sensor element (16 mm), so the sensor aperture may attenuate these very high frequencies.

[19] The focal mechanism, source time history, and absolute size of these foreshocks are quantified by comparing recorded signals to synthetic seismograms:

$$s(t) = G_{ki,j}(t) * M_{ij}(t) * i_k(t), \qquad (1)$$

where $*$ denotes convolution, $G_{ki,j}$ is the first spatial derivative of the elastodynamic Green's function, M_{ij} is the moment tensor, and $i_k(t)$ is the instrument response function for the piezoelectric sensors, which was verified in situ using ball impact calibration sources [*McLaskey and Glaser*, 2012]. Elastodynamic Green's functions $G_{ki,j}(t)$ were computed with a generalized ray theory code for an infinite slab [*Hsu*, 1985]. This code includes both near-field and far-field terms and was verified with 3-D finite element models. The Green's functions are valid for short time periods before reflections from the side edges of the sample pollute recorded signals. We model the granite sample as a homogeneous linear elastic material with $c_p = 4080$ m/s and $c_s = 2700$ m/s. Attenuation (Q) is not negligible but is not yet explicitly modeled in this work. Because it primarily affects high frequencies, attenuation has only a minor effect on moment magnitude (M_w) estimates described below.
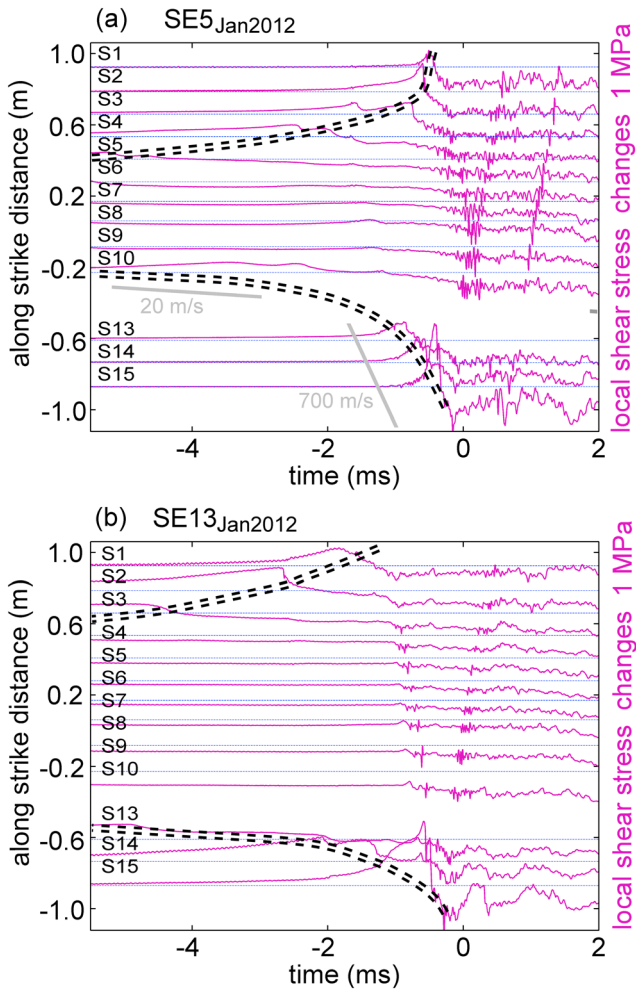
Figure 7. Local shear stress changes during nucleation phases iii and iv show the interaction between the expanding nucleation zone and the sample edges which are located at along strike distances of ±1 m. Thick dashed lines indicate the approximate location of the edge of the expanding slipping region. (a) An example of a more rapidly nucleating stick-slip instability which has a smaller sized nucleation zone that expands at a rate of ~700 m/s before reaching the edge of the sample. (b) An example of a stick-slip instability that nucleates more slowly and has a larger nucleation zone that reaches the sample edges before accelerating to seismic speeds.

### 3.2.2. Foreshock Locations and Characteristics

[20] The locations of foreshock hypocenters on the fault cross section are shown in Figure 8. The circles and diamonds denote the locations of foreshocks from the experiments conducted in January 2012 and November 2011, respectively. The size of the circles (or diamonds) matches the approximately ±10 mm location uncertainty in both along strike and depth dimensions. As shown, the locations of individual foreshocks persistently cluster on localized fault patches within the interior of the fault (labeled P0–P8). Figure 6b shows the output from piezoelectric sensor PZ4 high-pass filtered at 200 kHz to highlight the high-frequency foreshocks. The number below each foreshock corresponds to the fault patch where the foreshock

originated. Many of the stick-slip instabilities produced a similar sequence of foreshocks during nucleation phase ii. This sequence starts on Patch P1 near the bottom center of the fault. From there, the foreshock locations migrate along strike at a velocity of ~5–50 m/s which is roughly the same velocity as the expansion of slipping region during nucleation phases ii and iii, but is still 2 orders of magnitude slower than the velocity of migrating sources of high frequency observed during dynamic rupture when the entire fault surface slips. The relatively slow expansion of the slipping region during nucleation is qualitatively consistent with v_{slow} reported in other recent spontaneous nucleation experiments [*Nielsen et al.* 2010].

[21] Moment tensor inversion was not performed. Instead, the source properties of the individual foreshocks were estimated from forward modeling by comparing full-waveform synthetic seismograms to recorded signals in the ~50–300 kHz frequency band. First, we assumed that the time history of each component of $M_{ij}(t)$ was identical such that $M_{ij}(t) = p(t)M_{ij}$. We estimated $p(t)$ from the shape of the initial P wave arrivals detected at a variety of sensors. Then, by trial and error, we estimated M_{ij} by choosing from double couple, compensated linear vector dipole, and isotropic sources, as well as rotated versions and linear combinations of these forms. The suitability of a given M_{ij} was assessed based on the polarity and relative amplitude of both P and S waves felt by at least six sensors. For all of the well-constrained foreshocks studied, the focal mechanisms are consistent with that of a shear dislocation on the fault (i.e., a double couple with one of the two nodal planes oriented parallel to the fault) rather than an opening crack, explosion, or implosion. We cannot rule out the possibility that a small fraction of the seismic moment is due to isotropic or opening crack mechanisms, but it is unlikely that this fraction exceeds about 20% because it would thus alter the polarity or relative amplitude of the P and S waves enough to be easily identified in the waveforms.

[22] The characteristics of foreshocks produced by a given fault patch are similar between different stick-slip cycles. For example, Patches P2–P5 consistently produce $M_w \sim -6$ to -6.5 foreshocks with source durations less than 4 μs, while Patches P1 and P6 always produce more complex extended-duration foreshocks which consist of multiple $M_w \sim -6$ to -5 bursts of moment release. Figure 9a shows recorded signals and synthetic seismograms (dotted lines) for a short duration, $M_w = -6.3$ Patch P2 foreshock modeled as a 3 μs pulse of moment rate (peak moment rate of 300,000 Nm/s). The short-duration (~3–10 μs) foreshocks produce ground displacements with pulse-shaped far-field P and S waves. This indicates that the time history of $M_{ij}(t)$ is a step-like function. The duration of the nonzero part of $d(M_{jk}(t))/dt$ is defined as the source duration. Figure 9b illustrates a more complex, extended-duration Patch P6 foreshock modeled as a 15 μs $M_w = -5.3$ pulse followed, 130 μs later, by another 24 μs $M_w = -4.9$ pulse in moment rate. Foreshocks of this type have source time functions that are typically ~100–200 μs in total and are often composed of multiple ~20 μs bursts of moment release, each of which is moderately well modeled with a shear dislocation focal mechanism.

[23] The recorded waveforms from many of the foreshocks were similar enough in the 100 to 500 kHz frequency band that relative source locations could be attained by means of
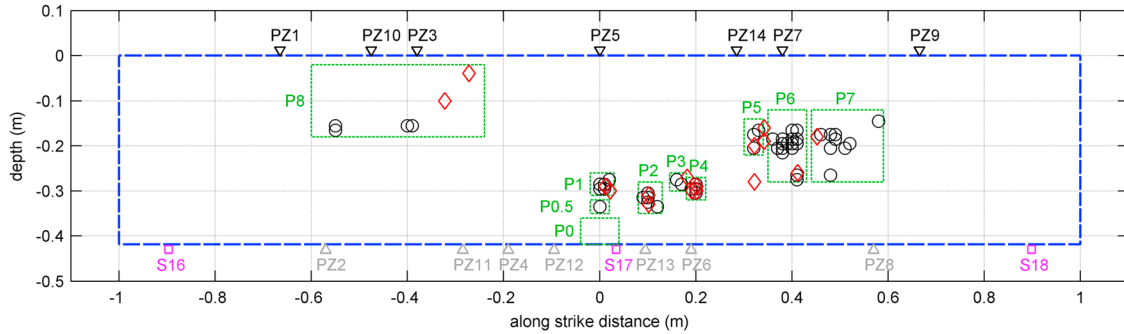
Figure 8. The dashed line indicates the fault cross section showing foreshock hypocenters and sensor locations. Smaller dotted rectangles denote fault sections labeled Patches P0–P8. Over many stick-slip cycles, foreshock hypocenters tend to cluster on those fault patches. Circles and diamonds denote locations of foreshocks from experiments conducted in January 2012 and November 2011, respectively. The circle (or diamond) size matches the approximately ±10 mm location uncertainty.

a cross-correlation technique. For each fault patch, we designated a template event—a foreshock that was cleanly recorded by many different stations. Then, at each station, we used cross correlation to calculate the phase difference between the waveform of the template event and that of a trial event (both waveforms were band-pass filtered from 100 to 500 kHz). For foreshocks emanating from Patches P2–P5, the phase difference between template events and trial events was constant to within 400 ns over all of the stations, which indicates that these foreshocks are indeed collocated (to a precision of less than 1 mm). Because the source time functions of foreshocks emanating from Patch P1 and P6 were more variable, the cross-correlation technique could not be used.

[24] The earliest, shortest-duration, and largest amplitude foreshocks are the easiest to identify and analyze because they are preceded by relative quiescence. Lower frequency or complex, extended-duration foreshocks, especially those buried in the coda of previous events, are more difficult to identify and interpret. In all of the stick-slip events studied, the final stages of nucleation produce complex, extended-duration foreshocks which continue to occur at a faster and faster rate and with larger and larger amplitudes until they are indistinguishable from the seismic waves generated during the dynamic rupture of the entire fault. These seismic signals are not readily interpreted with equation (1) and will be the focus of future studies. Patches P7 and P8 are the locations on the fault where the seismicity appears to transition from "foreshock" behavior (i.e., discrete pulses of moment release) to "main shock" behavior (i.e., more continuous radiation of high-frequency seismic waves) (see Figure 5). For the faster-nucleating events, this transition occurs closer to the center on Patch P7. For the slower-nucleating stick-slip events, the transition occurs somewhat further toward the ends of the sample and discrete foreshocks can be located on Patches P7 and P8 (see Figure 7). The ends of the fault appear to remain locked and aseismic during nucleation but do radiate seismic energy during dynamic rupture. Most of the central part of the fault remains aseismic during nucleation despite the fact that it accumulates ~10 μm of slip during this period.

3.2.3. Lower Frequency Seismicity

[25] Much of the seismicity recorded does not fit neatly into the above category either because it appears to be deficient in high frequencies or because the source duration is extended in time and lacks abrupt high-frequency wave arrivals. When considering lower frequencies, the wavelengths are comparable to the sample size and the boundary conditions and the resonance of the sample in the apparatus plays an increasingly important role. The piezoelectric sensors were calibrated in the lower frequency range (<5 kHz) by using a laser Doppler vibrometer as a reference sensor. In this range, the piezoelectric sensor sensitivity decreases and the output becomes a combination of displacement and velocity.

[26] An example of lower frequency ground motions associated with the nucleation process is shown in Figure 10. These 1–10 ms period ground motions are especially visible just prior to the high-frequency foreshock on Patch P1 (at −3 to 0 ms in Figure 10b). The amplitudes and polarities of these low-frequency motions are not consistent with those expected from elastodynamic sources (equation (1)). We do observe a four-lobed pattern of subsidence and uplift indicative of a shear dislocation, but the time history of these low-frequency ground deformations is nearly identical at all stations, and instead of a $1/r$ amplitude decay due to geometrical spreading, the amplitudes decay more rapidly outside of an ~200 mm radius zone surrounding the source. The relative amplitudes and polarities of the deformations at a given time are generally consistent with quasi-static deformations associated with relatively slow fault slip. We suspect that these deformations are the result of a sudden increase in the slip rate (i.e., a slip transient) on a centimeter-scale section of the fault. Due to the inexact fit of the quasi-static model used to interpret these observations and the rough calibration of the sensors in this low-frequency range, the spatial qualities of the slip transient are only constrained to an approximately 1–20 cm zone, but the timing of the slip transient is very well constrained and is described in more detail in section 3.3. In general, the duration of the recorded slip transients is 6–12 ms (Figure 10d), approximately 3 orders of magnitude longer than the source duration of the high-frequency foreshocks.

[27] Figure 10a shows the Patch 1 foreshock ground motions (from SE5$_{Jan2012}$) with a zoomed-in time scale and zoomed-out amplitude scale to show the first motions of the Patch P1 foreshock. Note that in Figures 10a and 10b, we display the signal from PZ10 to PZ14 inverted. These sensors are located on the opposite side of the fault from PZ1 to PZ9.
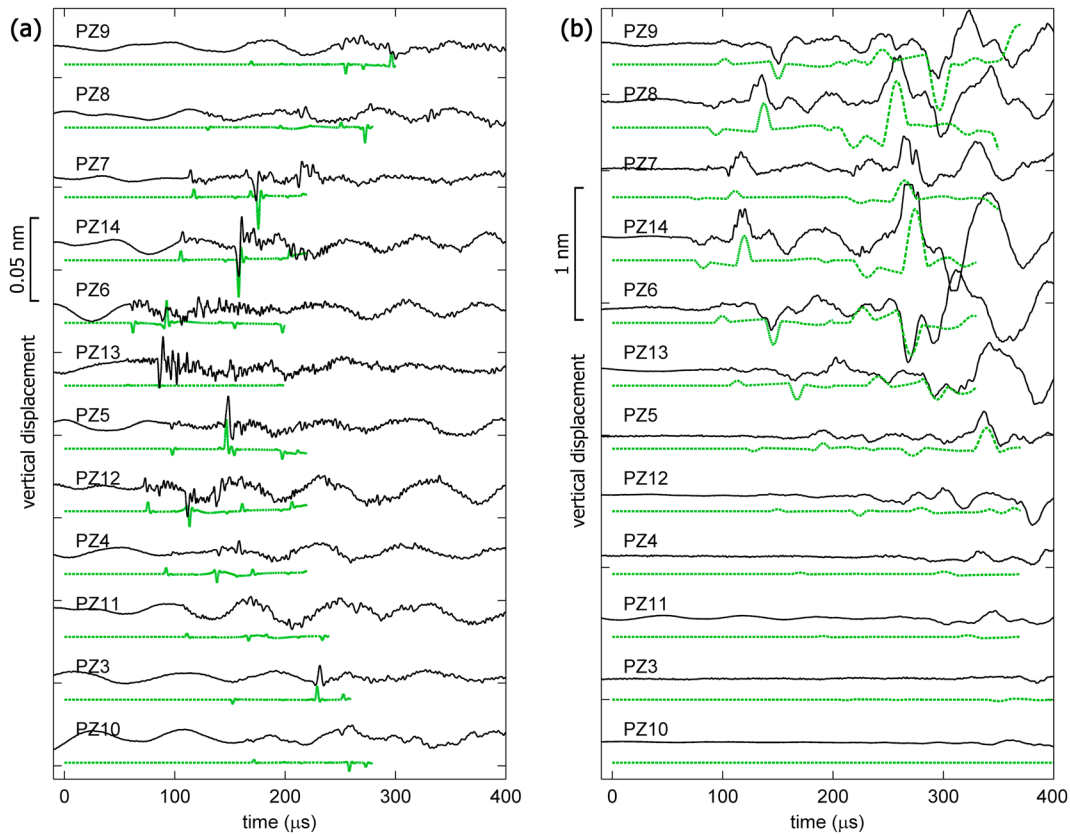
Figure 9. Examples of vertical ground displacements from two different foreshocks which occurred during the nucleation of stick-slip instability $SE12_{Jan2012}$ recorded with the array of piezoelectric sensors (PZ1–PZ14). The dashed lines are synthetic seismograms which are used to constrain the focal mechanism, time history, and absolute amplitude of the foreshocks. (a) A smaller and more impulsive foreshock emanating from Patch P2 modeled as a 3 µs, $M_w = -6.3$ pulse in moment rate. (b) A more complex, extended-duration Patch P6 foreshock modeled as a 15 µs, $M_w = -5.3$ pulse in moment rate followed, 130 µs later, by another 24 µs, $M_w = -4.9$ pulse in moment rate. The relatively long period noise in Figure 9a is a mild resonance of the sensor model at about 12 kHz which was excited by the previous, larger (Patch P1) foreshock.

3.3. Aseismic Slip and Foreshock Interaction

[28] To better understand the relationship between aseismic slip and foreshock occurrence, we carefully analyze local stress changes and ground motions associated with the beginning of nucleation phase ii and compare the different stick-slip cycles. Figure 10c shows the unfiltered output from PZ4 (gray) alongside the same signal filtered in two different ways. The black line is high-pass filtered at 200 kHz and magnified 10X to highlight the foreshocks. The green line is low-pass filtered at 2.5 kHz to highlight the time history of the slip transient. Figure 10d compares the high-passed PZ4 signal (black) and the low-passed PZ4 (green) and PZ6 (blue) signals with the shear stress measured by strain gage pair S17 (red) in small time windows surrounding the Patch 1 foreshock for many different stick-slip events.

[29] In all cases, the shear stress at S17 (near the bottom center of the fault) drops in two episodes. The first drop in stress is accompanied by an increase in the rate of the slip transient and is likely due to aseismic slip on Patch P0. Between the two episodes, shear stress at S17 levels off to a nearly constant value while the rate of the slip transient slows. The second stress drop occurs just after the foreshock. Coincident with the time of the foreshock, there is a step-like increase in the shear stress at S17 and a rapid increase in the rate of the slip transient.

[30] These observations describe a complicated interaction between seismic and aseismic slip, described qualitatively and schematically in Figures 10e and 10f. Aseismic slip commences on Patch P0, centered between PZ4 and PZ6. This slip causes local shear stress to drop in the slipping region (near S17) but causes shear stress to increase in surrounding areas. When the expanding aseismic slip transient encounters the stronger Patch P1 (Figure 10e), it slows and encircles it, and a stress concentration develops there. When the stress on the stronger Patch P1 exceeds the strength (Figure 10f), it slips seismically (unstably and very rapidly). The step-like increase in shear stress at S17 indicates that shear stress dropped extremely rapidly at P1 and was shed to neighboring regions, including P0, near S17. This stress increase in the region surrounding P1 causes the aseismic slip to continue at a faster rate and shear stress at S17 to drop further. Similar, more muted perturbations in stress at S17 and slip transients detected with PZ4 and PZ6 are coincident with later foreshocks. Low-frequency surface motions detected on the top surface of the sample with PZ5 and PZ7 (not shown in Figure 10d but visible between 17 and 23 ms in Figure 10b)
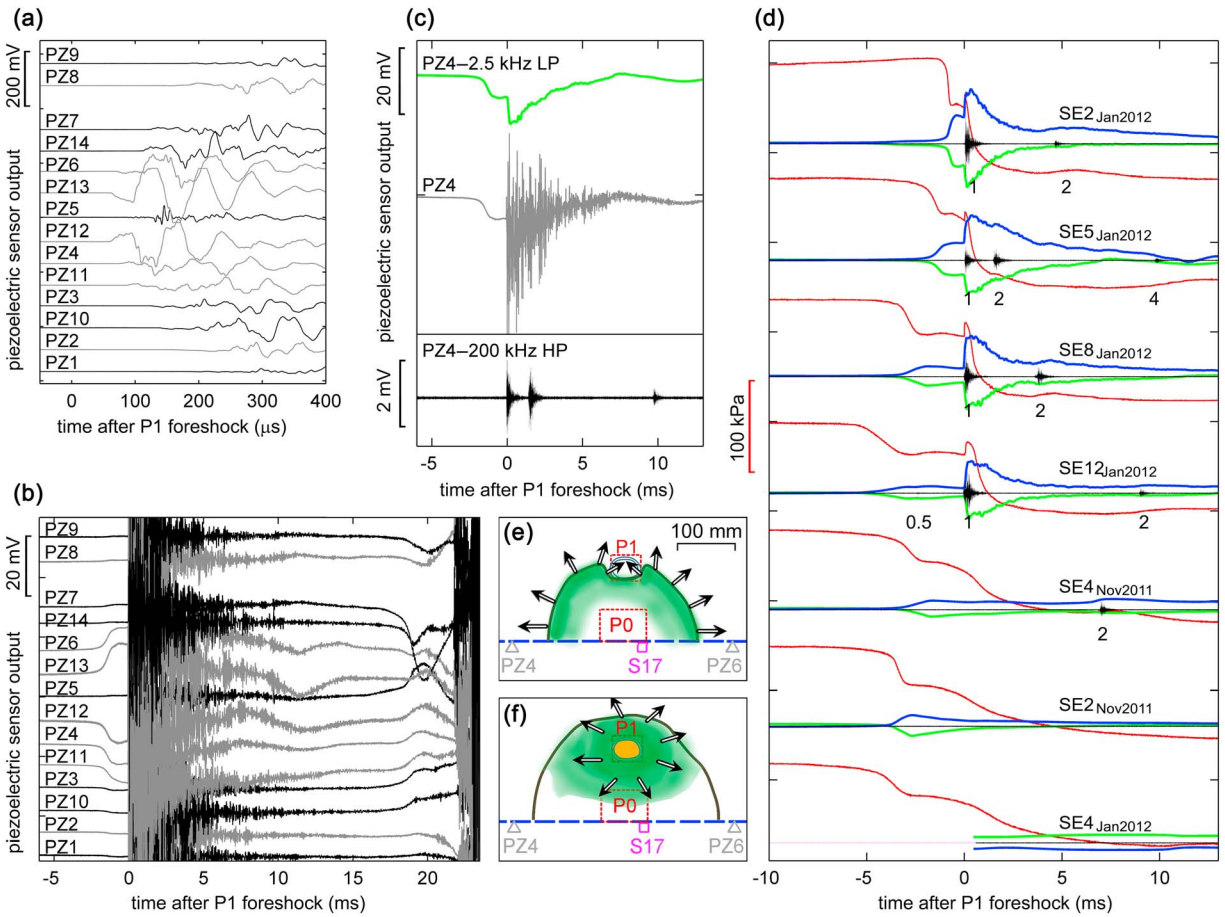
Figure 10. Low-frequency ground deformations indicative of an aseismic slip transient and comparison with associated foreshocks and stress changes. Ground motions associated with SE5$_{Jan2012}$ recorded with the piezoelectric sensor array at different time and amplitude scales. (a) Ground motions associated with the high-frequency Patch P1 foreshock. Sensor output is nearly proportional to vertical ground displacement in this high-frequency band. (b) When we zoom out in time and zoom in in amplitude, the low-frequency deformation due to aseismic slip transients can be seen 1–3 ms before the P1 foreshock as well as after 17 ms. (c) The unfiltered output from PZ4 taken from Figure 10b is shown in gray alongside the same signal filtered two different ways: low-pass filtered at 2.5 kHz to highlight the slip transient (green), and high-pass filtered at 200 kHz and magnified 10X to highlight the foreshocks (black). (d) Local shear stress at S17 (red) is shown alongside high-passed (black) and low-passed (green) PZ4 as well as the low-passed PZ6 (blue) for time windows centered on the Patch P1 foreshock for many different stick-slip instabilities. For those stick-slip instabilities that did not produce a Patch P1 foreshock, the time axis is roughly centered on the time when Patch 1 slipped aseismically. Black numbers beneath the signals denote the patch numbers where the foreshock hypocenters are located. (e–f) Schematic diagrams describing the interaction between aseismic and seismic slip. Green (orange) shading indicates aseismic (seismic) slip and arrows indicate associated stress redistribution (see text).

indicate the occurrence of slip transients near P5. These slip transients are closely followed by foreshocks on P5 and P6.

[31] The Patch P1 foreshock sequence described above was detected prior to the more rapidly nucleating stick-slip events (SE2, SE5–SE8, and SE12), but was not detected during the slower nucleation sequences (i.e., SE3, SE4, SE9, SE10, SE13, etc.) during the January 2012 tests. For both events with and without foreshocks, stress at S17 drops in two episodes and there is an inflection point between these episodes which indicates that aseismic slip was slowed momentarily. Events without foreshocks show no step-like increase in stress, and the subsequent drop in stress is somewhat more gradual, indicating that the absence of the

foreshock caused aseismic slip to progress more slowly than it would have otherwise.

3.4. When Foreshocks Are Not Detected and Repeatability of the Experiments

[32] No high-frequency foreshocks were detected before nucleation phase ii. Also, as previously mentioned, the Patches P1–P5 foreshock sequence was not detected during the slower nucleation sequences. As best we could ascertain, there are also no high-frequency aftershocks. The high frequencies (>80 kHz) of such aftershocks would have been easily discernible above the low-frequency (~200 Hz) ringing of the sample in the apparatus, which persists above the
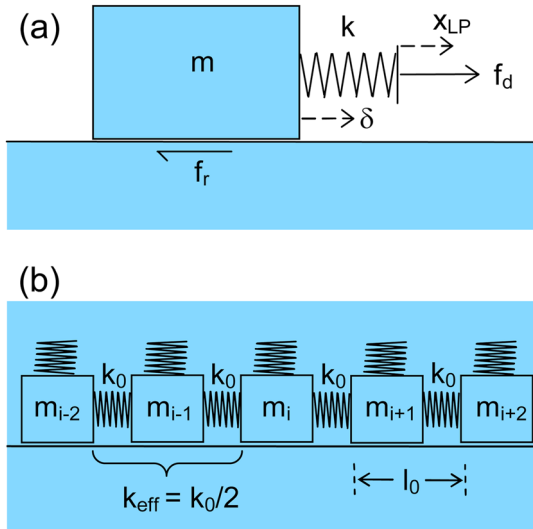
Figure 11. Frictional stability idealized with a simple slider block model. (a) The rigid block is pulled along a planar surface by means of a deformable spring of stiffness k. The spring applies the driving force f_d while motion is resisted by the force of friction f_r. (b) A deformable elastic continuum can be idealized as a series of rigid blocks connected by deformable springs of stiffness k_0 which depends on the block spacing l_0 and material rigidity.

noise level for about 250 ms after each slip event. Nevertheless, it is possible that some aftershocks escaped detection in the first 10 ms immediately after dynamic rupture. In this time period, high-amplitude, low-frequency ringing of the sample in the apparatus caused the output from the piezoelectric sensors to exceed the small digitization range described in section 2.2. Consequently, in the first 10 ms, the search for aftershocks was performed on the lower resolution signals recorded with the large digitization range (detection threshold $M_w \sim -5$). (The increased high-frequency noise level of the PZ4 data from 0 to 9 ms in Figure 6b is not due to aftershocks. It is digitization noise associated with the large digitization range, which was substituted for the small digitization range during this time period.)

[33] Output from the piezoelectric sensors was recorded in triggered mode, and though all of the detected P1 foreshocks were strong enough to trigger the recording system, it is still possible that some small ($M_w < -6$) foreshocks or aftershocks could have escaped detection because they did not trigger the recording system. To test this, we ran two more sequences of stick-slip events in May and August 2012. In these tests, the piezoelectric sensor output was recorded both continuously at 5 kHz and in triggered mode at 5 MHz with the triggering criterion set so that no high-frequency seismicity above $M_w \sim -7$ could escape detection. Most of the stick-slip events in the May and August 2012 sequences were extremely similar to earlier recorded events. As before, we detected high-frequency $M_w -4$ to -6.5 foreshocks only in the 5–50 ms before dynamic rupture, and low-frequency deformations indicative of collated aseismic slip were always detected before any high-frequency seismicity. With the more sensitive triggering criterion, we did sporadically detect some small amplitude signals during the early parts of the

loading phase, especially prior to the first stick-slip event of the sequence, but these signals could be identified only on the recordings from one or two of the sensors, so we were unable to verify that these signals were of mechanical origin rather than from electrical noise or that they were emanating from the fault rather than from the sample edges. Therefore, with a detection threshold of $M_w \sim -6.5$, we verified that no coherent earthquake-like sources were produced in the minutes before and after the stick-slip instability except those occurring in the final tens of milliseconds before stick slip, as reported in section 3.2.2. Additionally, no low-frequency ground motions indicative of aseismic slip transients were detected except in the same time period. One exception to the above statements is that we do occasionally detect a few $M_w \sim -6$ foreshocks and aftershocks in the seconds surrounding the first stick-slip event of a sequence. This first stick-slip event is typically abnormal in that it is smaller than usual and does not nucleate the same way as the stick-slip events described in section 3.1.

4. Discussion

[34] Many characteristics of the seismicity observed in the experiments reported in this paper appear to be similar to those of natural earthquakes, including the foreshock focal mechanisms, spatial clustering, triggering of seismicity by aseismic slip [e.g., *Segall et al.*, 2006], and the fact that foreshocks occur sometimes but not always. One exception is that there are typically no aftershocks. This might not be surprising given that the entire fault slips during each stick-slip instability and there is essentially no measurable afterslip, but it is also possible that the smooth and planar nature of the simulated fault and the lack of off-fault damage or the lack of fluids in the current experiments could contribute to the observed lack of aftershocks.

[35] When envisioning the way a fault might begin to slip, one might intuitively think that because a microscopically rough fault has many micrometer-sized contacts, they will slide past each other and produce many small seismic events. The consequence of h*, a minimum length scale for unstable fault slip (described below), is that this is not the case. Throughout most of the stick-slip experiments reported here, the laboratory fault is aseismic, despite the fact that portions of it slip up to 10 μm during the nucleation period. We estimate that the high-frequency foreshocks account for less than 1% of total moment released during nucleation phases ii and iii.

4.1. Frictional Stability and Minimum Earthquake Size

[36] The idea of a minimum earthquake size stems from observations and analyses of a rigid slider block pulled along a planar surface by means of a spring of stiffness *k*, as depicted in Figure 11a [*Ruina* 1983; *Rice and Ruina*, 1983]. Slip δ of the block is resisted by a friction force f_r. The driving force the spring exerts on the block has the form:

$$f_d = k(x_{LP} - \delta), \qquad (2)$$

where x_{LP} is the displacement of the load point which pulls the spring. Stick-slip instabilities require that (1) f_r is slip weakening (i.e., $df_r/d\delta < 0$) and (2) when the block begins to slip, the spring force is not relieved as fast as the friction force is reduced, i.e., $df_r/d\delta < df_d/d\delta$. If, on the other hand, $df_r/d\delta > df_d/d\delta$, then an incremental amount of slip will be

enough to keep $f_d < f_r$ and the block will never slip faster than $v_{LP} = \mathrm{d}x_{LP}/\mathrm{d}t$ (i.e., it will slide stably). The stiffness of the loading system is defined as

$$k \equiv \mathrm{d}f_d/\mathrm{d}\delta, \qquad (3)$$

so we can interpret the above discussion in terms of a critical spring stiffness $k_{cr} = -\mathrm{d}f_r/\mathrm{d}\delta$. For $k > k_{cr}$, the block slides stably; for $k < k_{cr}$, stick-slip motion is observed [e.g., *Dieterich*, 1978; *Ruina* 1983; *Rice and Ruina*, 1983; *Baumberger et al.*, 1994].

[37] The slider block stability concept can be applied to a fault patch located on a fault embedded in an elastic continuum of constant rigidity μ, as depicted in Figure 11b. In this case, we can define the effective stiffness of a fault patch as

$$k_{\mathrm{eff}} = \alpha\mu/h, \qquad (4)$$

where α is a geometrical constant with units of area, μ is the shear modulus, and h is the linear dimension of the slipping region. If only a small length of the fault slips (e.g., m_i from Figure 11) while the neighboring fault patches (m_{i-1} and m_{i+1}) remain locked, then the effective stiffness of the fault patch is relatively high ($h = l_0$ so $k_{\mathrm{eff}} = \alpha\mu/l_0$). If neighboring fault patches are also allowed to slip, and the total size h of the slipping region increases, then the effective stiffness of the fault patch at the center of the slipping region will be reduced (e.g., $h = 2l_0$ so $k_{\mathrm{eff}} = \alpha\mu/2l_0$). By reorganizing equation (4) and substituting k_{cr} for k_{eff}, we find a critical length scale:

$$h^* = \alpha\mu/k_{cr}, \qquad (5)$$

where only fault patches larger than h^* can slip unstably relative to their neighbors. If the rate-state constitutive relationship is assumed, then the critical length scale can be quantified [*Rice and Ruina*, 1983; *Dieterich*, 1986; *Dieterich*, 1992; *Rice* 1993]:

$$h^*_{r-s} = \mu\eta D_c/(\sigma_n(b-a)), \qquad (6)$$

where η is a geometric factor of order 1, D_c is the characteristic length scale over which friction evolves, and $(b-a)$ is the rate-state velocity weakening parameter. While the precise form of the rate-state parameter is somewhat debated [e.g., *Ampuero and Rubin*, 2008], the general form of equations (5) and (6) and the concept of a minimum length scale for instability is valid for any slip-weakening constitutive law where f_r is a continuous function of δ.

[38] Testing equation (6) and the concepts behind it was a motivating factor for the original construction of the 2 m biaxial apparatus used in the current experiments [*Dieterich*, 1981]. Indeed, the meter-sized region of accelerating aseismic slip observed in nucleation phase iii just before the stick-slip instability (Figures 3c and 7) is generally consistent with h^*_{r-s} [*Okubo and Dieterich*, 1984; *Dieterich and Kilgore*, 1996]. On the other hand, the tiny foreshocks we record are 2 to 3 orders of magnitude smaller.

4.2. Heterogeneity and an Asperity Model of a Foreshock

[39] The rate-state earthquake nucleation models described in section 1 suggest that fault slip near the nucleation zone gradually and smoothly accelerates from very low velocities up to seismic slip speeds on the order of 0.1 m/s. In the current experiments, measurements from the strain gages and slip sensors seem to corroborate with this description; it appears that fault slip accelerates relatively smoothly in the nucleation zone (i.e., Figure 4) and stress changes vary smoothly over >200 mm spatial scales (i.e., Figure 3c). If the radiation of seismic energy is simply proportional to fault slip velocity, then we might expect to record seismic waves that smoothly increase in amplitude as the fault slip accelerates in the final milliseconds before dynamic rupture. Instead, we see seismicity that begins in fits and starts. Discrete bursts of seismicity (foreshocks) 3–200 µs in duration are followed by tens of milliseconds of seismic quiescence. The pulse-shaped waveforms of the foreshocks indicate that only small patches of the fault are radiating seismic waves and only for very short time periods (3–25 µs), yet simultaneous measurements of stress changes, slip, and surface deformation all indicate that large portions of the fault are slipping.

[40] The foreshock observations described above, and particularly the apparent interaction between the foreshocks and aseismic slip described in section 3.3, evoke a foreshock model where a locked fault patch is loaded by the quasi-stable and aseismic slip of the surrounded region (i.e., an exterior crack instead of an expanding crack) [*Beeler et al.*, 2001; *Johnson and Nadeau*, 2002; *Chen and Lapusta*, 2009]. Models of this type typically require the seismogenic patch to be rheologically distinct from the surrounding fault (e.g., a steady state velocity weakening patch surrounded by steady state velocity strengthening material). The Sierra white granite samples used in the present experiments are homogeneous and do not permit mineralogical variations larger than the grain scale, so we speculate that the approximately millimeter-centimeter-scale strength heterogeneity implied by the foreshock clustering is simply caused by a slight topographic mismatch of the interacting fault surfaces, where normal stress and shear strength are higher than the surrounding fault sections. Prior to running the experiments, the fault blocks are lapped against each other to assure that the surfaces are well mated, so any surface irregularities must have survived the lapping procedure. After many stick-slip cycles, surface topography could encourage rheological heterogeneity by means of variations in gouge layer thickness. On natural faults, the presence of fluids may encourage clay minerals to accumulate in aseismically slipping regions while the locked and seismogenic patches retain the frictional properties of the surrounding fault rocks. Thus, with continued fault slip, surface topography (millimeter to centimeter in the current experiments and up to hundreds of meters on natural faults) could encourage rheological heterogeneity. The current laboratory samples have been in use for more than 25 years, and the fault has not been opened in 5 years, so it is possible that considerable heterogeneity has developed. In a future study, we intend to open the fault, separate the two halves of the sample, and measure surface roughness and gouge layer thickness.

[41] In the current experiments, the slipping region that surrounds the seismogenic foreshock patch slips quasi-stably and aseismically not because it is a steady state velocity strengthening material, but because the length scales are smaller than h^*_{r-s} and are thus too small to permit instability.

But what causes the foreshock patch to slip unstably and radiate seismic waves despite the fact that it is smaller than h^*_{r-s}? One possibility is that the seismogenic foreshock patch has higher normal stress and/or smaller D_c (i.e., it is smoother) than the surrounding fault, and this could effectively cause h^* to shrink. Another possibility is that the geometric factor η is smaller for an exterior crack geometry than for an interior crack. Yet it is difficult to imagine how these factors alone could allow a fault patch 2 orders of magnitude smaller than h^*_{r-s} to slip unstably relative to the surrounding fault sections.

4.3. Validity of the Constitutive Law

[42] Another possible explanation for the occurrence of the tiny foreshocks in light of the large h^*_{r-s} might be that the rate-state constitutive law is not valid. If the foreshocks are the result of tensile fracture or some similar material failure, then h^* might not apply. For example, acoustic emissions (AE) are routinely recorded in geophysical experiments that employ very slow loading conditions. Though a limited number of studies explore the physical mechanisms behind AE, they are often associated with tensile cracking or the brittle destruction of surface topography [e.g., *Stanchits and Dresen*, 2003; *Manthei*, 2005; *Thompson et al.*, 2009; *McLaskey and Glaser*, 2011]. But many characteristics of the foreshocks reported in this paper are different from typical acoustic emissions and more similar to natural earthquakes. For example, the foreshocks all have shear-type focal mechanisms and persistently occur at identical fault locations (to ~1 mm resolution) over at least 10 stick-slip cycles and 1.4 mm of cumulative slip. Additionally, foreshock characteristics do not appear to evolve with cumulative fault slip, but depend, to a large extent, on the speed of the aseismic slip that drives them. Based on these observations, we argue that the general form of the rate-state constitutive law remains valid, even on the approximately millimeter to centimeter scale of the foreshock patches.

4.4. Stressing Rate Dependence

[43] As described in section 3.4, the foreshocks only occur at the very latest stages of the nucleation process when accelerating aseismic slip produces local stressing rates of at least 20 MPa/s (e.g., S8 shown in Figure 6), significantly higher than the globally applied 0.001 MPa/s supplied by the flat jacks. We detect no coherent seismicity at earlier stages in the nucleation process which indicates that the tiny earthquakes cannot spontaneously nucleate on their own, but must be rapidly driven by stress changes induced by the aseismic slip of neighboring fault patches, else the fault will slip aseismically. We therefore propose that increased stressing rate effectively causes a dramatic and localized reduction in h*.

[44] Some insight into this mechanism can be gained by considering the spring-and-slider-block framework shown in Figure 11. For example, equation (3) implicitly and unrealistically assumes that x_{LP} is constant with respect to δ. To include this loading rate dependence, we consider some small amount of time dt over which the load point displaces an amount d$x_{LP} = v_{LP}$dt and the block slips an amount d$\delta = v$dt, where v is the average slip velocity of the block over dt. We can then update

equation (2) to read d$f_d = k(v_{LP}$d$t - v$d$t)$, and by the chain rule, equation (3) becomes

$$\mathrm{d}f_d/\mathrm{d}\delta = \mathrm{d}f_d/\mathrm{d}t \cdot \mathrm{d}t/\mathrm{d}\delta = k(v_{LP} - v) \cdot 1/v = k(v_{LP}/v - 1). \quad (7)$$

If v_{LP} is small compared to v, then equation (7) approaches equation (3). But if v_{LP} is large or v is small, then the effective stiffness is reduced and instability is encouraged. A similar result was reached by *Gu et al.* [1984], who showed that if pushed sufficiently far from steady state, a slider block can slip unstable even if $k > k_{cr}$. We can adapt equation (7) to the case of a fault in an elastic continuum (Figure 11b) by replacing v with v_i, and v_{LP} with $v_{i-1} + v_{i+1}$, where v_i is the slip velocity of fault patch m_i.

[45] While heterogeneity must be required to produce a foreshock—an instability within a larger, stably slipping region—observations presented in section 3.3 suggest that a high stressing rate is also necessary to force the small foreshock patch to radiate seismically, rather than slip aseismically. If this model is correct, then earthquakes with apparent dimensions significantly smaller than h^*_{r-s} can occur. The conclusion that h^* can be effectively reduced by loading conditions is also supported by numerical modeling. *Kaneko and Lapusta* [2008] showed that loading conditions could cause the nucleation zone size to shrink by an order of magnitude.

[46] This stressing-rate-dependent mechanism for seismic radiation may help explain the physics of tectonic tremor and why it appears to be repeatedly radiated by discrete fault patches [e.g., *Shelly et al.*, 2006, *Ghosh et al.*, 2012]. Even if the fault conditions where tremor occurs prohibit large earthquakes from nucleating, a sudden increase in the stressing rate on a fault patch in that region (due to the passage of a slow slip front) may be enough to cause that patch to slip unstably and radiate seismic waves in the form of a low-frequency earthquake.

[47] A rate dependence to frictional stability may also help explain observations of repeating earthquake sequences which sometimes show an increase in seismic moment (in addition to a decrease in recurrence time) immediately following a large nearby earthquake [*Chen et al.*, 2010; *Matsuzawa et al.*, 2012]. For example, if afterslip from the nearby earthquake causes a dramatic increase in the loading rate on the fault patch that hosts the repeating earthquakes, this could cause the surrounding fault sections, which would have otherwise slipped aseismically, to radiate seismically and contribute to an increase in the observed seismic moment of the earthquake.

4.5. Foreshock Triggering and V_{slow}

[48] The foreshocks appear to trigger one another, but in a delayed fashion. For example, with few exceptions, Patches P2–P5 do not produce foreshocks unless P1 produced a foreshock. The relatively long time delays (5 ms) between successive foreshocks compared to the spatial separation of their hypocenters (100 mm) indicate that foreshocks are not immediately triggered by the passage of seismic waves. Instead, it appears that the foreshocks indirectly trigger one another by hastening the slow and aseismic slip that drives them. In other words, if a foreshock patch is driven to fail seismically, then its coseismic stress changes encourage the very slip that produced it, and this will increase the chances

that another foreshock will occur. Because the laboratory fault is dry, these results reiterate that fluids are not required for delayed triggering of earthquakes and that diffusion-like temporal migration of earthquake locations can be explained by slowly expanding aseismic slip that results from a (dry) friction law such as rate-state friction [*Dieterich*, 1994; *Ando and Imanishi*, 2011].

[49] In the current experiments, foreshock hypocenters roughly track the expansion of the nucleation zone, which expands at a velocity of 5–50 m/s. The hypocenters of foreshock swarms that precede some large earthquakes on natural faults do not show such a clear or monotonic expansion [*Abercrombie et al.*, 1995]. It is possible that off-fault seismicity produces added complexity to foreshock patterns on natural faults. We believe that the expansion of the slipping region observed in nucleation phase iii just prior to dynamic rupture reported here is the same as v_{slow} reported in other studies [*Nielsen et al.*, 2010; *Kaneko and Ampuero*, 2011]. Our observations suggest that v_{slow} is not a material constant but is systematically affected by the same factors that affect other characteristics of the nucleation process. These factors include the initial fault stress levels and the way that stress and strength vary over time and space due to time-dependent strengthening mechanisms (i.e., healing) and aseismic fault slip.

4.6. Scaling of Laboratory Results and Scaling of D_c

[50] If no scaling is applied, then the foreshocks reported here represent a sequence of $M_w -5$ to -6.5 events that occur 2–50 ms prior to and within the nucleation zone of an $\sim M_w -2$ event. If such an event occurred in the Earth and was monitored from a station tens of meters away, the foreshocks might be completely undetectable or might manifest themselves as a small moment release a few tens of milliseconds prior to the main moment release [e.g., *Ellsworth and Beroza*, 1995]. Alternatively, if some of the laboratory fault properties are different from field conditions, then the nucleation and associated foreshocks could occur over drastically different length and time scales. While the elastic properties (rigidity, density, and elastic wave speed) of the granite samples are similar to crustal materials that host natural faults, we would expect normal stress and temperature of the seismogenic crust to be higher than in the laboratory. Natural faults may also have somewhat different friction properties due to differing mineralogy, or due to the presence of fluids. For example, the presence of clay minerals in the fault zone can produce a rate-state velocity weakening parameter $(b - a)$ which is close to zero or even negative, and this can increase h^*_{r-s} or even prevent unstable and seismogenic slip from occurring altogether (see equation (6)) [*Lockner et al.*, 2011]. Finally, and perhaps most importantly for the current experiments, natural faults may be much rougher than the saw cut-and-lapped fault surfaces of the laboratory samples. Exhumed faults that are accessible to inspection are much rougher and contain more gouge than most lab faults (for reviews, see *Marone* [1998] and *Rice and Cocco* [2007]). Rougher faults with thick gouge layers have larger D_c [e.g., *Biegel et al.*, 1989; *Marone et al.*, 1990], and this could significantly affect the length and time scales over which nucleation develops. *Okubo and Dieterich* [1984] conducted laboratory experiments that demonstrated how a rougher fault with a larger D_c has a larger nucleation

zone and must slip more and over a longer time duration before dynamic rupture commences. If D_c on the lab fault is smaller than on natural faults, then the laboratory experiments described here may serve as high-speed, small-scale models of seismic and aseismic interactions.

[51] When modeling earthquakes, small values of D_c are sometimes chosen to keep h^*_{r-s} smaller than the smallest observed earthquakes [*Lapusta and Rice*, 2003; *Kaneko and Lapusta*, 2008]. This modeling decision is motivated by the assumption that earthquake dimensions must be larger than h^*_{r-s}, but the current experiments seem to show that fault heterogeneity and rapid stressing rates can produce earthquakes with apparent source dimensions significantly smaller than h^*. If the same is true on natural faults, this implies that there are physical differences between earthquakes of different sizes based on their dimensions relative to h^*_{r-s}. These differences may not be obvious from the analysis of seismic waves. Instead, they might be identified by nucleation conditions. For example, an earthquake with apparent dimensions smaller than h^*_{r-s} cannot be the result of spontaneous nucleation on an otherwise locked fault that is loaded at a tectonic loading rate. Instead, such a small earthquake must be the result of relatively rapid stress changes either due to a nearby larger earthquake (i.e., aftershocks or foreshocks), anthropogenic sources such as mining activity, fluid injection, or reservoir construction, or it must be driven by a larger-scale aseismic slip transient.

5. Conclusion

[52] Our results show that heterogeneity of fault strength can cause local instabilities (slip transients) to occur within the nucleation zone of a larger stick-slip event, and sometimes these instabilities become so severe that they radiate seismically and produce foreshocks. The foreshocks we record persistently occur on specific fault patches that are ~ 2–70 mm in size. The fault patches that generate these tiny ($M_w = -5$ to -6.5) earthquakes are much smaller than h^*_{r-s}, the critical length scale for unstable fault slip. Therefore, we propose that frictional stability is modulated by stressing rate, such that a fault patch that is stronger than its surroundings (but smaller than h^*_{r-s}) can radiate seismically if it is rapidly loaded (i.e., 20 MPa/s) by quasi-stable and aseismic slip of neighboring fault sections. The foreshocks we observe do not spontaneously occur on their own; they are a by-product of the nucleation process of a larger stick-slip instability and they indirectly trigger one another by hastening the aseismic slip transients that produce them.

[53] These lab observations may provide some physical insight into the mechanics of foreshocks, particularly short-term foreshocks and tremor-like signals sometimes observed to emanate from the eventual hypocenter of a larger earthquake [e.g., *Bouchon et al.*, 2011; *Tape et al.*, 2013]. Stressing rate dependence to frictional stability may help explain the radiation of tectonic tremor and certain characteristics of repeating earthquake sequences [*Matsuzawa et al.*, 2012]. Similar rate-dependent mechanisms may help explain the existence of extremely small earthquakes recorded at the San Andreas Fault

Observatory at Depth and in deep gold mines [*Ellsworth et al.*, 2007; *Boettcher et al.*, 2009; *Kwiatek et al.*, 2010].

References

Abercrombie, R. E., D. C. Agnew, and F. K. Wyatt (1995), Testing a model of earthquake nucleation, *Bull. Seismol. Soc. Am.*, 85, 1873–1878.

Ampuero, J.-P., and A. M. Rubin (2008), Earthquake nucleation on rate and state faults: Aging and slip laws, *J. Geophys. Res.*, 113, B01302, doi:10.1029/2007JB005082.

Ando, R., and K. Imanishi (2011), Possibility of M_w 9.0 main shock triggered by diffusional propagation of after-slip from M_w 7.3 foreshock, *Earth Planets Space*, 63, 767–771, doi:10.5047/eps.2011.05.016.

Baumberger, T., F. Heslot, and B. Perrin (1994), Crossover from creep to inertial motion in friction dynamics, *Nature*, 367, 544–546.

Beeler, N. M., D. A. Lockner, and S. H. Hickman (2001), A simple stick-slip and creep slip model for repeating earthquakes and its implication for microearthquakes at Parkfield, *Bull. Seismol. Soc. Am.*, 91, 1797–1804.

Beeler, N. M., B. Kilgore, A. McGarr, J. Fletcher, J. Evans, and S. R. Baker (2012), Observed source parameters for dynamic rupture with non-uniform initial stress and relatively high fracture energy, *J. Struct. Geol.*, 38, 77–89.

Biegel, R. L., C. G. Sammis, and J. H. Dieterich (1989), The frictional properties of a simulated gouge having a fractal particle distribution, *J. Struct. Geol.*, 11, 827–846.

Bouchon, M., H. Karabulut, M. Aktar, S. Ozalaybey, J. Schmittbuhl, and M. P. Bouin (2011), Extended nucleation of the 1999 M_w 7.6 Izmit earthquake, *Science*, 331, 877–880.

Boettcher, M. S., A. McGarr, and M. Johnston (2009), Extension of Gutenberg-Richter distribution to M_w–1.3, no lower limit in sight, *Geophys. Res. Lett.*, 36, L10307, doi:10.1029/2009GL038080.

Boettcher, M., and J. McGuire (2009), Scaling relations for seismic cycles on mid-ocean ridge transform faults, *Geophys. Res. Lett.*, 36, L21301, doi:10.1029/2009GL040115.

Chen, K. H., R. Burgmann, R. M. Nadeau, T. Chen, and N. Lapusta (2010), Postseismic variations in seismic moment and recurrence interval of repeating earthquakes, *Earth Planet. Sci. Lett.*, 299, 118–125.

Chen, T., and N. Lapusta (2009), Scaling of small repeating earthquakes explained by interaction of seismic and aseismic slip in a rate and state fault model, *J. Geophys. Res.*, 113, B01311, doi:10.1029/2008JB005749.

Chiaraluce, L., L. Valoroso, D. Piccinini, R. Di Stefano, and P. De Gori (2011), The anatomy of the 2009 L'Aquila normal fault system (central Italy) imaged by high resolution foreshock and aftershock locations, *J. Geophys. Res.*, 116, B12311, doi:10.1029/2011JB008352.

Dieterich, J. H. (1978), Preseismic fault slip and earthquake prediction, *J. Geophys. Res.*, 83, 3940–3948.

Dieterich, J. H. (1979), Modeling of rock friction: 1. Experimental results and constitutive equations, *J. Geophys. Res.*, 84, 2161–2168.

Dieterich, J. H. (1981), Potential for geophysical experiments in large scale tests, *Geophys. Res. Lett.*, 8, 653–656.

Dieterich, J. H. (1986), A model for the nucleation of earthquake slip, in *Earthquake Source Mechanics, Geophys. Monogr. Ser.*, vol. 37, edited by S. Das, J. Boatwright, and C. H. Scholz, pp. 37–47, AGU, Washington, D. C.

Dieterich, J. H. (1992), Earthquake nucleation on faults with rate- and state-dependent friction, *Tectonophysics*, 211, 115–134.

Dieterich, J. H. (1994), A constitutive law for rate of earthquake production and its application to earthquake clustering, *J. Geophys. Res.*, 99, 2601–2618.

Dieterich, J. H., and B. D. Kilgore (1996), Implications of fault constitutive properties for earthquake prediction, *Proc. Natl. Acad. Sci. U. S. A.*, 93, 3787–3794.

Dodge, D. A., G. C. Beroza, and W. L. Ellsworth (1995), Foreshock sequence of the 1992 Landers, California, earthquake and its implications for earthquake nucleation, *J. Geophys. Res.*, 100, 9865–9880.

Dodge, D. A., G. C. Beroza, and W. L. Ellsworth (1996), Detailed observations of California foreshock sequences: Implications for the earthquake initiation process, *J. Geophys. Res.*, 101, 22,371–22,392.

Ellsworth, W., and G. C. Beroza (1995), Seismic evidence for an earthquake nucleation phase, *Science*, 268, 851–855.

Ellsworth, W., S. H. Hickman, M. D. Zoback, K. Imanishi, C. H. Thurber, and S. Roecker (2007). Micro-, nano-, and picoearthquakes at SAFOD: Implications for earthquake rupture and fault mechanics, Eos Trans. AGU, 88(52), Fall Meet. Suppl., Abstract S12B-05.

Fang, Z., J. H. Dieterich, and G. Xu (2010), Effect of initial conditions and loading path on earthquake nucleation, *J. Geophys. Res.*, 115, B06313, doi:10.1029/2009JB006558.

Geller, R. J. (1997), (1997) Earthquake prediction: A critical review, *Geophys. J. Int.*, 131, 425–450.

Ghosh, A., J. E. Vidale, and K. C. Creager (2012), Tremor asperities in the transition zone control evolution of slow earthquakes, *J. Geophys. Res.*, 117, B10301, doi:10.1029/2012JB009249.

Gu, J.-C., J. R. Rice, A. L. Ruina, and S. T. Tse (1984), Slip motion and stability of a single degree of freedom elastic system with rate and state dependent friction, *J. Mech Phys. Solids*, 32, 167–196.

Hsu, N. (1985), Dynamic Green's functions of an infinite plate—A computer program, *Tech. Rep. NBSIR 85–3234,* Cent. for Manuf. Eng., Natl. Bur. of Stand., Gaithersburg, Md.

Johnson, L. R., and R. M. Nadeau (2002), Asperity model of an earthquake: Static problem, *Bull. Seismol. Soc. Am.*, 92, 672–686.

Johnston, M. J. S., R. D. Borcherdt, A. T. Linde, and M. T. Gladwin (2006), Continuous borehole strain and pore pressure in the near field of the 28 September 2004 M_w 6.0 Parkfield, California, earthquake: Implications for nucleation, fault response, earthquake prediction, and tremor, *Bull. Seismol. Soc. Am.*, 96(4B), S56–S72.

Kaneko, Y., and N. Lapusta (2008), Variability of earthquake nucleation in continuum models of rate-and-state faults and implications for aftershock rates, *J. Geophys. Res.*, 113, B12312, doi:10.1029/2007JB005154.

Kaneko, Y., and J.-P. Ampuero (2011), A mechanism for preseismic steady rupture fronts observed in laboratory experiments, *Geophs. Res. Lett*, 38, L21307, doi:10.1029/2011GL049953.

Kwiatek, G., K. Plenkers, M. Nakatani, Y. Yabe, G. Dresen, and JAGUARS-Group (2010), Frequency-magnitude characteristics down to magnitude −4.4 for induced seismicity recorded at Mponeng gold mine, South Africa, *Bull. Seismol. Soc. Am.*, 100, 1165–1173.

Lapusta, N., and Y. Liu (2009), Three-dimensional boundary integral modeling of spontaneous earthquake sequences and aseismic slip, *J. Geophys. Res.*, 114, B09303, doi:10.1029/2008JB005934.

Lapusta, N., and J. R. Rice (2003), Nucleation and early seismic propagation of small and large events in a crustal earthquake model, *J. Geophys. Res.*, 108(B4), 2205, doi:10.1029/2001JB000793.

Lengline, O., J. E. Elkory, G. Daniel, J. Schmittbuhl, R. Toussaint, J.-P. Ampuero, and M. Bouchon (2012), Interplay of seismic and aseismic deformations during earthquake swarms: An experimental approach, *Earth Planet. Sci. Lett.*, 331–332, 215–223.

Lewis, M. A., and Y. Ben-Zion (2007), Examination of scaling between proposed early signals in P waveforms and earthquake magnitudes, *Geophys. J. Int.*, 171, 1258–1268.

Lockner, D. A., P. G. Okubo, and J. H. Dieterich (1982), Containment of stick slip failures on a simulated fault by pore fluid injection, *Geophys. Res. Lett.*, 9, 801–804.

Lockner, D. A., and P. G. Okubo (1983), Measurements of frictional heating in granite, *J. Geophys. Res.*, 88, 4313–4320.

Lockner, D., C. Morrow, D. Moore, and S. Hickman (2011), Low strength of deep San Andreas Fault gouge from SAFOD core, *Nature*, 472, 82–85.

Manthei, G. (2005), Characterization of acoustic emission sources in a rock salt specimen under triaxial compression, *Bull. Seismol. Soc. Am.*, 95, 1674–1700.

Marone, C., C. B. Raleigh, and C. H. Scholz (1990), Frictional behavior and constitutive modeling of simulated fault gouge, *J. Geophys. Res.*, 95, 7007–7025.

Marone, C. (1998), Laboratory-derived friction laws and their application to seismic faulting, *Annu. Rev. Earth Planet. Sci.*, 26, 643–646.

Marsan, D., and B. Enescu (2012), Modeling the foreshock sequence prior to the 2011, M_w9.0 Tohoku, Japan, earthquake, *J. Geophys. Res.*, 117, B06316, doi:10.1029/2011JB009039.

Matsuzawa, T., K. Shimamura, T. Okada, and N. Uchinda (2012), Unusual rupture pattern of off-Kamaishi repeaters after the 2011 Tohoku earthquake, Abstract S21B-2499 presented at 2012 Fall Meeting, AGU, San Francisco, Calif.

McGuire, J. J., M. S. Boettcher, and T. H. Jordan (2005), Foreshock sequences and short-term earthquake predictability on East Pacific Rise transform faults, *Nature*, 434, 457–461.

McLaskey, G. C., and S. D. Glaser (2011), Micromechanics of asperity rupture during laboratory stick slip experiments, *Geoph. Res. Lett.*, 38, L12302, doi:10.1029/2011GL047507.

McLaskey, G. C., and S. D. Glaser (2012), Acoustic emission sensor calibration for absolute source measurements, *J Nondest. Eval.*, 31(2), 157–168.

Miyazaki, S., J. J. McGuire, and P. Segall (2011), Seismic and aseismic fault slip before and during the 2011 Tohoku earthquake, *Earth Planets Space*, *63*(7), 637–642.

Nadeau, R. M., and L. R. Johnson (1998), Seismological studies at Parkfield VI: Moment release rates and estimates of source parameters for small repeating earthquakes, *Bull. Seismol. Soc. Am.*, *88*, 790–814.

Nielsen, S., J. Taddeucci, and S. Vinciguerra (2010), Experimental observation of stick-slip instability fronts, *Geophys. J. Int.*, *180*, 697–702.

Obara, K. (2002), Nonvolcanic deep tremor associated with subduction in southwest Japan, *Science*, *296*, 1679–1681.

Ohnaka, M., and Y. Kuwahara (1990), Characteristic features of local breakdown near a crack-tip in the transition zone from nucleation to unstable rupture during stick-slip shear failure, *Tectonophysics*, *175*, 197–220.

Ohnaka, M., and L. F. Shen (1999), Scaling of the shear rupture process from nucleation to dynamic propagation: Implications of geometric irregularity of the rupturing surfaces, *J. Geophys. Res.*, *104*, 817–844.

Okubo, P. G., and J. H. Dieterich (1984), Effects of physical fault properties on frictional instabilities produced on simulated faults, *J. Geophys. Res.*, *89*, 5817–5827.

Rice, J. R. (1993), Spatio-temporal complexity of slip on a fault, *J. Geophys. Res.*, *98*, 9885–9907.

Rice, J. R., and M. Cocco (2007), Seismic fault rheology and earthquake dynamics, in *Tectonic Faults: Agents of Change on a Dynamic Earth*, edited by M. R. Handy, G. Hirth, and N. Hovius, chap. 5, pp. 99–137, MIT Press, Cambridge, Mass.

Rice, J. R., and A. Ruina (1983), Stability of steady frictional slipping, *J. Appl. Mech.*, *50*, 343–349.

Rubin, A. M., and J.-P. Ampuero (2005), Earthquake nucleation on (aging) rate and state faults, *J. Geophys. Res.*, *110*, B11312, doi:10.1029/2005JB003686.

Ruina, A. (1983), Slip instability and state variable friction laws, *J. Geophys. Res.*, *88*, 10,359–10,370.

Segall, P., E. Desmarais, D. Shelly, A. Miklius, and P. Cervelli (2006), Earthquakes triggered by silent slip events on Kilauea volcano, Hawaii, *Nature*, *442*, 71–74.

Shelly, D. R., G. C. Beroza, S. Ide, and S. Nakamula (2006), Low-frequency earthquakes in Shikoku, Japan, and their relationship to episodic tremor and slip, *Nature*, *442*, 188–191.

Stanchits, S., and G. Dresen (2003), Separation of tensile and shear cracks based on acoustic emission analysis of rock fracture, paper presented at the symposium Non-Destructive Testing in Civil Engineering 2003 (NDT-CE), Deutche Gesellschaft fur Zerstorungsfreie Prufugn e.V. (DGZfP), Berlin.

Tape, C., M. West, V. Silwal, and N. Ruppert (2013), Earthquake nucleation and triggering on an optimally oriented fault, *Earth Planet. Sci. Lett.*, *363*, 231–241.

Thompson, B. D., R. P. Young, and D. A. Lockner (2009), Premonitory acoustic emissions and stick-slip in natural and smooth-faulted Westerly granite, *J. Geophys. Res.*, *114*, B02205, doi:10.1029/2008JB005753.

Tullis, T. E. (1996), Rock friction and its implications for earthquake prediction examined via models of Parkfield earthquakes, *Proc. Natl. Acad. Sci. U. S. A.*, *93*, 3803–3810.

Zanzerkia, E. E., G. C. Beroza, and J. E. Vidale (2003), Waveform analysis of the 1999 Hector Mine, California, foreshock sequence, *Geophys. Res. Lett.*, *30*(8), 1429, doi:10.1029/2002GL016383.